FROM LEADS TO LATENTS: ATTENTION-DRIVEN MASKED AUTOENCODER FOR ECG TIME SERIES

Samuel Ruiperez-Campillo[1],* Moritz Vandenhirtz[1],* Simon Böhi[2], Sonia Laguna[1], Irene Cannistraci[1], Andrea Agostini[1], Ece Ozkan[2], Thomas M. Sutter[1], Julia E. Vogt[1]
[1]Department of Computer Science, ETH Zurich, Switzerland
[2]Department of Biomedical Engineering, University of Basel, Switzerland

ABSTRACT

Electrocardiograms (ECGs) are among the most widely available clinical signals and play a central role in cardiovascular diagnosis. While recent foundation models have shown promise for learning transferable ECG representations, most existing pretraining approaches treat leads as independent channels and fail to explicitly leverage their strong structural redundancy. We introduce the latent attention masked autoencoder (LAMAE) framework that directly exploits this structure by learning cross-lead connection mechanisms during self-supervised pretraining. Our approach models higher-order interactions across leads through latent attention, enabling permutation-invariant aggregation and adaptive weighting of lead-specific representations. We provide empirical evidence on the Mimic-IV-ECG database that leveraging the cross-lead connection constitutes an effective form of structural supervision, improving representation quality and transferability. Our method shows strong performance in predicting ICD-10 codes, outperforming independent-lead masked modeling and alignment-based baselines.

1 INTRODUCTION

Cardiovascular diseases remain among the leading causes of death worldwide (Roth et al., 2025). Clinical diagnosis and monitoring increasingly rely on multimodal data streams including imaging, clinical notes, lab tests, and physiological signals, among which the electrocardiogram (ECG) is the most ubiquitous modality due to its cost-efficiency, non-invasiveness, and mature clinical interpretation pipelines (Kashou et al., 2023). Its automated diagnosis has been dominated for decades by expert-crafted features coupled with classical classifiers (Liu et al., 2014; Chen et al., 2018). Over the last years, deep learning has largely shifted the field toward end-to-end learning from raw ECGs, with convolutional neural networks (CNNs) (Ribeiro et al., 2020) and recurrent models (Übeyli, 2010) as the predominant architectures for many clinical tasks (Sau et al., 2024; Hannun et al., 2019).

More recently, foundation models have emerged as a compelling direction to reduce reliance on expensive medical labels and enable transfer across tasks and cohorts (Moor et al., 2023; Tian et al., 2024). Yet, frontier general-purpose models still lag behind domain experts on clinical benchmarks and remain costly to adapt or deploy in practice (Khan et al., 2025). A key reason is that most pretraining pipelines remain largely oblivious to domain structure, particularly in ECG time series, where such structure is particularly explicit. This structure is not a nuisance; it is an intrinsic self-supervisory signal that modern pretraining objectives rarely exploit directly and that motivates cross-lead representations rather than independent-lead designs.

Self-supervised learning (SSL) offers a scalable alternative to label-heavy supervision in medicine (Azizi et al., 2021; Moody et al., 2025; Manduchi et al., 2023). Masked autoencoders (MAEs) (He et al., 2022) have gained momentum by reconstructing missing content from sparse context, encouraging learning robust, transferable representations. In ECG specifically, masked modeling has been explored on an independent-lead basis (Na et al., 2024) and with language-inspired tokenization schemes (Jin et al., 2024). Yet, existing methods often tokenize using lead-specific encoders or treat leads as quasi-independent "channels", limiting their ability to learn cross-lead correspondence.

*Equal contribution. Correspondence to samuel.ruiperezcampillo@inf.ethz.ch.

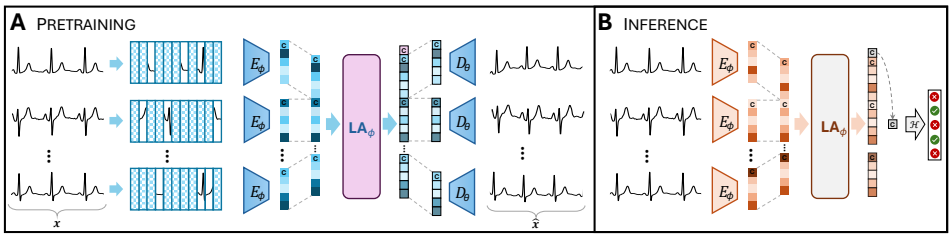

Figure 1: **Framework overview.** (left) Each ECG is separated into 12 leads, which are encoded separately and subsequently processed jointly through a latent attention transformer. The training objective is masked reconstruction. (right) The predictions are based on the latent attention's CLS token.

Leveraging the coherence of medical datasets, clinical recordings often come as structured multi-view observations that share anatomy and semantics across views. Exploiting this structure via multiview contrast, cross-modal alignment, or multitask learning (Laguna et al., 2025) can improve robustness and label efficiency in multimodal models (Mo & Liang, 2024; Pellegrini et al., 2025; Chen et al., 2024). Recently, Erlacher et al. (2025) combined multi-lead MAE reconstruction with a lead-alignment objective to enforce cross-lead consistency. While effective, such a pairwise alignment comes with limitations (Tschannen et al., 2023), which complicates design and may under-utilize richer, higher-order relationships among leads. In contrast, attention-based aggregation is a natural fit for structured latent sets: it supports permutation-invariant processing of variable-size collections while learning which elements are most informative (Lee et al., 2019) and has been shown to provide interpretable, instance-weighted summaries in related weakly supervised settings (Ilse et al., 2018).

In this work, we propose a multi-lead MAE framework that directly capitalizes on ECG structure by learning cross-lead connection mechanisms and modeling higher-order lead interactions by integrating latent attention. Concretely, our contribution is four-fold: (i) we introduce a multi-lead MAE with explicit cross-lead connection learning that leverages intrinsic redundancy across leads; (ii) we enhance the framework with latent attention to capture higher-order dependencies beyond pairwise alignment; (iii) we provide empirical arguments for cross-lead connection learning as a scalable form of structural supervision; and (iv) we demonstrate broad clinical translation spanning coarse ICD-based phenotyping to fine-grained disease classification.

2 Methods

We assume an ECG dataset $\mathbb{X} = \{\boldsymbol{X}^{(i)}\}_{i=1}^{N}$, where N is the number of ECG recordings in the dataset, $\boldsymbol{X}^{(i)} = \{\boldsymbol{x}_l^{(i)}\}_{l\in\mathbb{L}}$, $\mathbb{L}$ is the set of leads (e.g. 12 leads in our dataset $\mathbb{L} = \{\ell_I, \ell_{II}, \ell_{III}, \ell_{aVR}, \ell_{aVL}, \ell_{aVF}, \ell_{V_1}, \ell_{V_2}, \ell_{V_3}, \ell_{V_4}, \ell_{V_5}, \ell_{V_6}\}$ for our dataset (Strodthoff et al., 2024a) or see section A.

The proposed work extends the Masked Autoencoder method (He et al., 2022) to the ECG domain by introducing a self-attention module in the latent space, i.e., between the encoders E_ϕ and the decoders D_θ. We call the new module *Latent Attention* (LA).

2.1 Latent Attention for Multi-Lead Integration

Our latent attention module, inspired by Ilse et al. (2018); Lee et al. (2019), learns the correlation and shared information between different leads but is flexible enough to not having to merge information between leads in case it would be supoptimal.

We design the latent attention module as a multi-head, multi-layer self-attention block using an additional CLS token similar to the ViT architecture (Kolesnikov et al., 2021).

$$\boldsymbol{Z}_{out}^{(i)} = LA_\phi(\boldsymbol{Z}_{\text{vis}}^{(i)}) = LA_\phi(M_{\text{LA}}(\boldsymbol{Z}^{(i)})) = LA_\phi(M_{\text{LA}}(\{\boldsymbol{z}_l^{(i)}\}_{l\in\mathbb{L}})) \tag{1}$$

Similar to encoder E_ϕ in the MAE, we apply a random mask $M_{\text{LA}}(\cdot)$ to the input embeddings $\boldsymbol{Z}^{(i)}$, i.e., $\boldsymbol{Z}_{\text{vis}}^{(i)} = M_{\text{LA}}(\boldsymbol{Z}^{(i)})$ with a masking ratio α_{LA}. See section 2.2 for details on the masking process.

Table 1: ICD-10 code prediction performance by hierarchical group under linear probing of the corresponding backbones from the studied models. Best results in **bold** and second best in *italics*.

	Ours		Baselines			
ICD hierarchy	**LAMAE**	**LAMAE$_E$**	**Scratch**	**MMVM**	**Ind$_P$**	**Ind$_S$**
IX	*0.8345*	0.8340	0.7715	0.6771	**0.8380**	0.7776
IX.I05–I09	**0.8317**	*0.8278*	0.7408	0.5754	0.8259	0.7564
I07	*0.8772*	**0.8802**	0.8091	0.6804	0.8669	0.8310
I08	**0.8272**	*0.8263*	0.7523	0.6755	0.8235	0.7676
IX.I10–I1A	*0.7549*	**0.7570**	0.7043	0.5861	0.7506	0.7092
I11	0.8103	*0.8124*	0.7491	0.6283	**0.8163**	0.7602
I13	*0.8651*	**0.8704**	0.8106	0.6826	0.8655	0.8194
IX.I20–I25	**0.8046**	*0.7995*	0.7425	0.6182	0.7939	0.7508
I20	0.7880	**0.7963**	0.7147	0.6574	*0.7934*	0.7324
I21	0.8229	**0.8402**	0.7465	0.5585	*0.8265*	0.7542
IX.I26–I28	0.7399	*0.7474*	0.6948	0.5785	**0.7499**	0.6977
IX.I30–I5A	0.8624	*0.8624*	0.7955	0.6321	**0.8665**	0.8010
I35	0.7981	**0.8050**	0.7365	0.6246	*0.7983*	0.7423
I42	*0.8772*	**0.8838**	0.8396	0.7193	0.8731	0.8458
I44	0.9019	*0.9050*	0.8439	0.7591	**0.9091**	0.8467
I45	*0.8407*	**0.8493**	0.7766	0.6646	0.8392	0.7828
I46	0.8336	*0.8481*	0.7697	0.6562	**0.8523**	0.7809
I47	*0.8051*	0.8023	0.7409	0.6480	**0.8140**	0.7461
I48	0.8837	*0.8861*	0.7852	0.6952	**0.8927**	0.7933
I50	*0.8720*	**0.8747**	0.8166	0.6169	*0.8720*	0.8235
IX.I60–I69	0.6694	*0.6723*	0.6290	0.5473	**0.6823**	0.6348
IX.I70–I79	*0.7416*	**0.7441**	0.6942	0.5956	0.7440	0.6974
IX.I80–I89	0.6890	*0.6949*	0.6349	0.5731	**0.6985**	0.6324
IX.I95–I99	0.6772	*0.6782*	0.6224	0.5519	**0.6943**	0.6275

2.2 ECG-LAMAE

Different to previous works (Na et al., 2024; Jin et al., 2024), we use per-lead encoders E_ϕ and decoders D_θ with shared weights ϕ and θ. The latent attention module allows the model to learn the connection between the different leads to extract more meaningful information.

As in the standard MAE implementation, we only feed the visible tokens $\mathcal{T}_{\text{vis}}$ to the encoders E_ϕ, where $\mathcal{T}_{\text{vis}} \subseteq \{1, \ldots, T\}$ are the indices of the visible patches after applying $M_{\text{E}}(\cdot)$, i.e., $\boldsymbol{x}_{l_{\text{vis}}}^{(i)} = M_{\text{E}}(\boldsymbol{x}_l^{(i)})$. We therefore have $T_{\text{vis}} = |\mathcal{T}_{\text{vis}}| = (1 - \alpha_{\text{E}}) \cdot T$, where T is the total number of input tokens.

Using our latent attention module, we have the following objective function

$$\mathcal{L}\left(\boldsymbol{X}^{(i)}\right) = \frac{1}{\alpha_{\text{E}}} \frac{1}{|\mathbb{L}|} \sum_{l \in \mathbb{L}} \sum_{t \notin \mathcal{T}_{\text{vis}}} \left\| \boldsymbol{x}_{l_t}^{(i)} - \hat{\boldsymbol{x}}_{l_t}^{(i)} \right\|_2^2, \qquad \text{where} \qquad \hat{\boldsymbol{x}}_l^{(i)} = D_\phi(LA(\boldsymbol{Z}_{\text{vis}}^{(i)})_l)$$

and $\boldsymbol{Z}_{\text{vis}}^{(i)} = M_{\text{LA}}(\{\boldsymbol{z}_l^{(i)}\}_{l \in \mathbb{L}})$ is the set of all non-masked latent tokens $\boldsymbol{z}_l^{(i)}$ coming from all leads $\boldsymbol{x}_l^{(i)}$, i.e., $\boldsymbol{z}_l^{(i)} = E_\phi(\boldsymbol{x}_l^{(i)})$. This architecture supports the extraction of relevant information of each lead, combined with subsequent merging of the information in the latent attention module for a global representation captured within the CLS token. This token is then used for downstream tasks, as depicted in fig. 1 (right).

3 Experiments and Results

We evaluated multi-label ICD-10 prediction from 12-lead ECGs across Chapter IX (I00–I99), spanning valvular disease, hypertensive disease, ischemic syndromes and myocardial infarction, pulmonary circulation disorders, cardiomyopathies, conduction disease, atrial fibrillation/flutter, heart failure, and vascular/cerebrovascular conditions (table 1 and appendix sections A to C). Overall, LAMAE-based models achieve strong performance across granularities, with chapter-level AUROC ≈0.85 (after fine-tuning; table 4) and competitive linear-probing results (IX: 0.834; table 3). Performance is highest for ECG-salient phenotypes, notably conduction and rhythm disorders (e.g., I44 fine-tuning up to 0.9097; I48 up to 0.9016) and acute myocardial infarction subtypes (I21.* often >0.93; I210 up to 0.9749), consistent with stereotyped waveform signatures (PR/QRS abnormalities, irregular rhythm, ST/T changes). In contrast, broader vascular and cerebrovascular

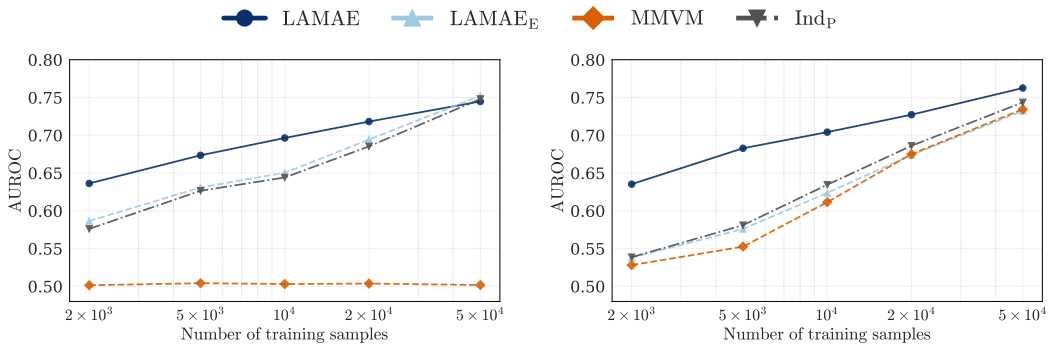

(a) Linear Probing (b) Finetuning

Figure 2: **Label efficiency under finetuning.** Performance curves of the macro-averaged AUROC over all 228 Chapter IX codes, as a function of the number of training studies used for finetuning.

groupings (I60–I69, I80–I89, I95–I99) are harder from waveform-only inputs (fine-tuning ∼0.69–0.72), plausibly reflecting weaker direct ECG imprint and higher label/context heterogeneity. Table 1 is supplemented by an exploration of fine-tuning performance (Tab. 4), which details the greater improvements over linear probing and highlights the benefit of the pretrained backbone for downstream adaptationm, as well as the fine-grained hierarchy results for linear probing in Tab.3.

Scaling experiments show that gains from structure-informed pretraining concentrate in scarce-data regimes (Fig. 2). Under linear probing and full fine-tuning, LAMAE outperforms scratch-trained and simpler baselines most strongly at small pretraining set sizes, with gaps narrowing only in large regimes (e.g., $\gtrsim$50k samples; Fig. 2). This supports latent attention as a structure-aware fusion mechanism over correlated lead projections: it can exploit redundancy to encode shared physiology, yielding more sample-efficient representations when curated cardiology datasets are limited.

A broader ICD-10 benchmarking study is provided by Strodthoff et al. (2024b). While not directly comparable, our fine-tuned AUROCs are in a similar range or higher for several overlapping, ECG-identifiable codes, including IX (0.8495), I132 (0.9119), I210 (0.9632), I447 (0.9452), and AF-related subcodes such as I481 (0.8902) and I482 (0.9312) (table 3). Strodthoff et al. (2024b) likewise reports strong results for conduction/AF-related codes (e.g., I440 and AF groupings). For the global burden of atrial fibrillation (ICD48 and 48.*; (Chugh et al., 2014)), our performance is superior to prior task-specific studies that report AUROCs around 0.82–0.85 across external cohorts with CNN-based models (Brant et al., 2025), and 0.67–0.8 using demographics or NN-extracted features on a 1-day ECG recording (Gadaleta et al., 2023). This is broadly consistent with AF being learnable yet sensitive to cohort shift and label timing. For conduction/heart block phenotypes related to I44 and sub-groups, reported performance varies widely across clinical settings ranging 0.594 to 0.889 (Sau et al., 2025), and our results with AUROC above 0.9 suggest that multi-lead structural pretraining can yield robust discrimination even under limited downstream data.

Limitations include the imperfect nature of ICD labels as proxies for physiology and the restricted clinical context available to waveform-only models, particularly for vascular/cerebrovascular diagnoses. Nevertheless, the consistent low-data gains and strong performance on ECG-salient phenotypes indicate that explicitly leveraging cross-lead structure via latent attention is a practical route toward more transferable ECG foundation representations.

4 Conclusion

We introduced LAMAE, a multi-lead masked autoencoder that injects structure into ECG pretraining via latent attention over lead-specific latents. Across a broad Chapter IX ICD-10 hierarchy, LAMAE yields strong AUROC under both linear probing and fine-tuning, with the largest advantages in low-data regimes and in diagnoses where multi-lead interactions are central. These results support that exploiting cross-lead redundancy as structural supervision can improve sample efficiency and downstream transfer, offering a scalable template for time-series foundation models, potentially beyond ECG, where observations naturally come as correlated sets of views. Even more, latent attention could serve as a general template wherever there is structure between measurement to be leveraged.

ACKNOWLEDGEMENTS

ACKNOWLEDGEMENTS

This work was supported under project IDs a150 and aa012 as part of the Swiss AI Initiative, through a grant from the ETH Domain and computational resources provided by the Swiss National Supercomputing Centre (CSCS) under the Alps infrastructure. MV and SL are supported by the Swiss State Secretariat for Education, Research, and Innovation (SERI) under contract number MB22.00047. TS and AA are supported by the grant #2021-911 of the Strategic Focal Area "Personalized Health and Related Technologies (PHRT)" of the ETH Domain (Swiss Federal Institutes of Technology).

REFERENCES

Shekoofeh Azizi, Basil Mustafa, Fiona Ryan, Zachary Beaver, Jan Freyberg, Jonathan Deaton, Aaron Loh, Alan Karthikesalingam, Simon Kornblith, Ting Chen, et al. Big self-supervised models advance medical image classification. In *Proceedings of the IEEE/CVF international conference on computer vision*, pp. 3478–3488, 2021. 1

Luisa CC Brant, Antônio H Ribeiro, Oseiwe B Eromosele, Marcelo M Pinto-Filho, Sandhi M Barreto, Bruce B Duncan, Martin G Larson, Emelia J Benjamin, Antonio LP Ribeiro, and Honghuang Lin. Prediction of atrial fibrillation from the ecg in the community using deep learning: A multinational study. *Circulation: Arrhythmia and Electrophysiology*, 18(10):e013734, 2025. 4

Xiaohe Chen, Yan Wang, Lirong Wang, et al. Arrhythmia recognition and classification using ecg morphology and segment feature analysis. *IEEE/ACM transactions on computational biology and bioinformatics*, 16(1):131–138, 2018. 1

Zhihong Chen, Maya Varma, Jean-Benoit Delbrouck, Magdalini Paschali, Louis Blankemeier, Dave Van Veen, Jeya Maria Jose Valanarasu, Alaa Youssef, Joseph Paul Cohen, Eduardo Pontes Reis, et al. Chexagent: Towards a foundation model for chest x-ray interpretation. In *AAAI 2024 Spring Symposium on Clinical Foundation Models*, 2024. 2

Sumeet S Chugh, Rasmus Havmoeller, Kumar Narayanan, David Singh, Michiel Rienstra, Emelia J Benjamin, Richard F Gillum, Young-Hoon Kim, John H McAnulty Jr, Zhi-Jie Zheng, et al. Worldwide epidemiology of atrial fibrillation: a global burden of disease 2010 study. *Circulation*, 129 (8):837–847, 2014. 4

Lucas Erlacher, Andrea Agostini, Samuel Ruiperez-Campillo, Ece Ozkan, Thomas M Sutter, and Julia E Vogt. Swissbeatsnet: A multilead masked autoencoder for chagas disease detection. *Computing In cardiology*, 15:16, 2025. 2

Matteo Gadaleta, Patrick Harrington, Eric Barnhill, Evangelos Hytopoulos, Mintu P Turakhia, Steven R Steinhubl, and Giorgio Quer. Prediction of atrial fibrillation from at-home single-lead ecg signals without arrhythmias. *npj Digital Medicine*, 6(1):229, 2023. 4

Ary L Goldberger, Luis AN Amaral, Leon Glass, Jeffrey M Hausdorff, Plamen Ch Ivanov, Roger G Mark, Joseph E Mietus, George B Moody, Chung-Kang Peng, and H Eugene Stanley. Physiobank, physiotoolkit, and physionet: components of a new research resource for complex physiologic signals. *circulation*, 101(23):e215–e220, 2000. 8

Brian Gow, Tom Pollard, Larry A Nathanson, Alistair Johnson, Benjamin Moody, Chrystinne Fernandes, Nathaniel Greenbaum, Jonathan W Waks, Parastou Eslami, Tanner Carbonati, et al. Mimic-iv-ecg: Diagnostic electrocardiogram matched subset. *Type: dataset*, 6:13–14, 2023. 8

Awni Y Hannun, Pranav Rajpurkar, Masoumeh Haghpanahi, Geoffrey H Tison, Codie Bourn, Mintu P Turakhia, and Andrew Y Ng. Cardiologist-level arrhythmia detection and classification in ambulatory electrocardiograms using a deep neural network. *Nature medicine*, 25(1):65–69, 2019. 1

Kaiming He, Xinlei Chen, Saining Xie, Yanghao Li, Piotr Dollár, and Ross Girshick. Masked autoencoders are scalable vision learners. In *Proceedings of the IEEE/CVF conference on computer vision and pattern recognition*, pp. 16000–16009, 2022. 1, 2

Maximilian Ilse, Jakub Tomczak, and Max Welling. Attention-based deep multiple instance learning. In *International conference on machine learning*, pp. 2127–2136. PMLR, 2018. 2

Jiarui Jin, Haoyu Wang, Hongyan Li, Jun Li, Jiahui Pan, and Shenda Hong. Reading your heart: Learning ecg words and sentences via pre-training ecg language model. In *International conference on learning representations*, 2024. 1, 3

Alistair EW Johnson, Lucas Bulgarelli, Lu Shen, Alvin Gayles, Ayad Shammout, Steven Horng, Tom J Pollard, Sicheng Hao, Benjamin Moody, Brian Gow, et al. Mimic-iv, a freely accessible electronic health record dataset. *Scientific data*, 10(1):1, 2023. 8

Anthony H Kashou, Peter A Noseworthy, Thomas J Beckman, Nandan S Anavekar, Michael W Cullen, Kurt B Angstman, Benjamin J Sandefur, Brian P Shapiro, Brandon W Wiley, Andrew M Kates, et al. Ecg interpretation proficiency of healthcare professionals. *Current problems in cardiology*, 48(10):101924, 2023. 1

Wasif Khan, Seowung Leem, Kyle B See, Joshua K Wong, Shaoting Zhang, and Ruogu Fang. A comprehensive survey of foundation models in medicine. *IEEE Reviews in Biomedical Engineering*, 2025. 1

Alexander Kolesnikov, Alexey Dosovitskiy, Dirk Weissenborn, Georg Heigold, Jakob Uszkoreit, Lucas Beyer, Matthias Minderer, Mostafa Dehghani, Neil Houlsby, Sylvain Gelly, Thomas Unterthiner, and Xiaohua Zhai. An image is worth 16x16 words: Transformers for image recognition at scale. 2021. 2

Sonia Laguna, Andrea Agostini, Alain Ryser, Samuel Ruiperez-Campillo, Irene Cannistraci, Moritz Vandenhirtz, Stephan Mandt, Nicolas Deperrois, Farhad Nooralahzadeh, Michael Krauthammer, et al. Structure is supervision: Multiview masked autoencoders for radiology. *arXiv preprint arXiv:2511.22294*, 2025. 2

Juho Lee, Yoonho Lee, Jungtaek Kim, Adam Kosiorek, Seungjin Choi, and Yee Whye Teh. Set transformer: A framework for attention-based permutation-invariant neural networks. In *International conference on machine learning*, pp. 3744–3753. PMLR, 2019. 2

Yun Liu, Zeeshan Syed, Benjamin M Scirica, David A Morrow, John V Guttag, and Collin M Stultz. Ecg morphological variability in beat space for risk stratification after acute coronary syndrome. *Journal of the American Heart Association*, 3(3):e000981, 2014. 1

Laura Manduchi, Moritz Vandenhirtz, Alain Ryser, and Julia Vogt. Tree variational autoencoders. *Advances in Neural Information Processing Systems*, 36:54952–54986, 2023. 1

Shentong Mo and Paul Pu Liang. Multimed: Massively multimodal and multitask medical understanding. *arXiv preprint arXiv:2408.12682*, 2024. 2

Jonathan B Moody, Alexis Poitrasson-Rivière, Jennifer M Renaud, Tomoe Hagio, Fares Alahdab, Mouaz H Al-Mallah, Michael D Vanderver, Sascha N Goonewardena, Edward P Ficaro, and Venkatesh L Murthy. A foundation transformer model with self-supervised learning for ecg-based assessment of cardiac and coronary function. *NEJM AI*, 2(12):AIoa2500164, 2025. 1

Michael Moor, Oishi Banerjee, Zahra Shakeri Hossein Abad, Harlan M Krumholz, Jure Leskovec, Eric J Topol, and Pranav Rajpurkar. Foundation models for generalist medical artificial intelligence. *Nature*, 616(7956):259–265, 2023. 1

Yeongyeon Na, Minje Park, Yunwon Tae, and Sunghoon Joo. Guiding masked representation learning to capture spatio-temporal relationship of electrocardiogram. In *International conference on learning representations*, 2024. 1, 3

Chantal Pellegrini, Ege Özsoy, Benjamin Busam, Benedikt Wiestler, Nassir Navab, and Matthias Keicher. Radialog: Large vision-language models for x-ray reporting and dialog-driven assistance. In *Medical Imaging with Deep Learning*, 2025. 2

Antônio H Ribeiro, Manoel Horta Ribeiro, Gabriela MM Paixão, Derick M Oliveira, Paulo R Gomes, Jéssica A Canazart, Milton PS Ferreira, Carl R Andersson, Peter W Macfarlane, Wagner Meira Jr, et al. Automatic diagnosis of the 12-lead ecg using a deep neural network. *Nature communications*, 11(1):1760, 2020. 1

Gregory A. Roth, Global Burden of Cardiovascular Diseases, and Risks 2023 Collaborators. Global, regional, and national burden of cardiovascular diseases and risk factors in 204 countries and territories, 1990-2023. *Journal of the American College of Cardiology*, 86(22):2167–2243, 2025. 1

Arunashis Sau, Libor Pastika, Ewa Sieliwonczyk, Konstantinos Patlatzoglou, Antonio H Ribeiro, Kathryn A Mcgurk, Boroumand Zeidaabadi, Henry Zhang, Krzysztof Macierzanka, Danilo Mandic, et al. Artificial intelligence-enabled electrocardiogram for mortality and cardiovascular risk estimation: a model development and validation study. *The Lancet Digital Health*, 6(11): e791–e802, 2024. 1

Arunashis Sau, Henry Zhang, Joseph Barker, Libor Pastika, Konstantinos Patlatzoglou, Boroumand Zeidaabadi, Ahmed El-Medany, Gul Rukh Khattak, Kathryn A McGurk, Ewa Sieliwonczyk, et al. Artificial intelligence–enhanced electrocardiography for complete heart block risk stratification. *JAMA cardiology*, 10(11):1092–1099, 2025. 4

Nils Strodthoff, JM Lopez Alcaraz, and W Haverkamp IV. Mimic-iv-ecg-ext-icd: Diagnostic labels for mimic-iv-ecg (version 1.0. 1). *PhysioNet. RRID: SCR_007345 https://doi. org/10.13026/hdyc-1h77*, 2024a. 2, 8

Nils Strodthoff, Juan Miguel Lopez Alcaraz, and Wilhelm Haverkamp. Prospects for artificial intelligence-enhanced electrocardiogram as a unified screening tool for cardiac and non-cardiac conditions: an explorative study in emergency care. *European Heart Journal-Digital Health*, 5 (4):454–460, 2024b. 4, 8

Yuanyuan Tian, Zhiyuan Li, Yanrui Jin, Mengxiao Wang, Xiaoyang Wei, Liqun Zhao, Yunqing Liu, Jinlei Liu, and Chengliang Liu. Foundation model of ecg diagnosis: Diagnostics and explanations of any form and rhythm on ecg. *Cell Reports Medicine*, 5(12), 2024. 1

Michael Tschannen, Manoj Kumar, Andreas Steiner, Xiaohua Zhai, Neil Houlsby, and Lucas Beyer. Image captioners are scalable vision learners too. *Advances in Neural Information Processing Systems*, 36:46830–46855, 2023. 2

Elif Derya Übeyli. Recurrent neural networks employing lyapunov exponents for analysis of ecg signals. *Expert systems with applications*, 37(2):1192–1199, 2010. 1

A MATERIALS

We conducted experiments on the MIMIC-IV-ECG-Ext-ICD resource (Strodthoff et al., 2024a), a PhysioNet (Goldberger et al., 2000)release that links raw 12-lead ECG waveforms from MIMIC-IV-ECG (Gow et al., 2023) to clinically grounded diagnostic labels from the corresponding MIMIC-IV Johnson et al. (2023) emergency department and inpatient records. Concretely, ECG acquisition timestamps are aligned with ED stays and hospital admissions to associate each recording with discharge diagnosis codes, providing ICD-10-CM label sets derived from routine clinical documentation rather than retrospective re-annotation. The dataset includes identifiers to retrieve additional clinical context (e.g., ED stay and hospital admission IDs), basic demographics (e.g., age-at-recording, sex), and fold assignments designed to avoid patient overlap for benchmarking and comparability across studies (Strodthoff et al., 2024a). In our study, only ECG raw waveforms and their paired ICD-10 code were used.

Following the benchmark framing introduced by Strodthoff et al. (2024b), we treat ICD-10-CM codes as multi-label targets at multiple granularities (chapter/block/category/subcategory), enabling evaluation from coarse phenotyping to fine-grained diagnosis. Where needed for consistency across label hierarchies, ICD codes may be normalized to a fixed digit format and expanded to include higher-level ancestors in the ICD tree, supporting hierarchical reporting and clinically meaningful aggregation (Strodthoff et al., 2024a;b).

B ON ICD CODES AND FURTHER DETAILS ON THOSE USED IN THIS STUDY

International Classification of Diseases (ICD) codes provide a standardized taxonomy for clinical diagnoses and are routinely used for billing, cohort definition, and large-scale observational research. In this work, we focus on ICD-10 Chapter IX (Diseases of the circulatory system; I00–I99), and report predictive performance at multiple levels of granularity: (i) the chapter-level aggregate, (ii) chapter blocks (e.g., I05–I09), (iii) 3-character categories (e.g., I07), and (iv) selected 4-character subcategories (e.g., I07.1; written as I071). This hierarchical evaluation reflects clinically meaningful groupings while enabling finer assessment of model behaviour on specific diagnoses. An extended description of the clinical meaning per code is included in table 2.

C SUPPLEMENTARY RESULTS: FINE-GRAINED ANALYSIS

Fine-grained Classification Results. In table 3, we present an extended analysis of the fine-grained classification performance initially discussed in table 1 on linear probing. The results demonstrate that performance trends remain remarkably consistent across the ICD-10 hierarchy. Notably, the relative advantages of our proposed methods are preserved even as the classification task becomes more granular, confirming the robustness of the learned representations.

Performance of LAMAE under Varying Supervision. Table 4 compares the performance of LAMAE and LAMAE$_E$ across both linear probing and fine-tuning regimes. While both models achieve competitive results under linear probing, fine-tuning LAMAE yields a significantly larger performance gain. This suggests that the pretrained backbone serves as a powerful initialization that can be further leveraged to maximize predictive accuracy when labeled data allows for full model updates.

Table 2: Clinical meaning of the ICD-10 Chapter IX codes reported in tables 1 and 3, shown with the same hierarchy.

ICD hierarchy	Clinical description
IX	Diseases of the circulatory system (I00–I99).
IX.I05–I09	Chronic rheumatic heart diseases (I05–I09).
I07	Rheumatic tricuspid valve diseases.
I071	I07.1 — Tricuspid (valve) insufficiency (rheumatic).
I078	I07.8 — Other tricuspid valve diseases.
I08	Multiple valve diseases (often rheumatic or unspecified origin).
I080	I08.0 — Disorders of both mitral and aortic valves.
I081	I08.1 — Disorders of both mitral and tricuspid valves.
I083	I08.3 — Combined disorders of mitral, aortic and tricuspid valves.
IX.I10–I1A	Hypertensive diseases (I10–I15).
I11	Hypertensive heart disease.
I13	Hypertensive heart and renal disease.
I130	I13.0 — Hypertensive heart and renal disease with (congestive) heart failure.
I132	I13.2 — Hypertensive heart and renal disease with both (congestive) heart failure and renal failure.
IX.I20–I25	Ischaemic heart diseases (I20–I25).
I20	Angina pectoris.
I200	I20.0 — Unstable angina.
I209	I20.9 — Angina pectoris, unspecified.
I21	Acute myocardial infarction.
I210	I21.0 — Acute transmural myocardial infarction of anterior wall.
I211	I21.1 — Acute transmural myocardial infarction of inferior wall.
I213	I21.3 — Acute transmural myocardial infarction of unspecified site.
I214	I21.4 — Acute subendocardial myocardial infarction.
IX.I26–I28	Pulmonary heart disease and diseases of pulmonary circulation (I26–I28).
IX.I30–I5A	Other forms of heart disease (ICD block: I30–I52; reported here as I30–I5A).
I35	Nonrheumatic aortic valve disorders.
I350	I35.0 — Aortic (valve) stenosis.
I359	I35.9 — Aortic valve disorder, unspecified.
I42	Cardiomyopathy.
I420	I42.0 — Dilated cardiomyopathy.
I428	I42.8 — Other cardiomyopathies.
I429	I42.9 — Cardiomyopathy, unspecified.
I44	Atrioventricular and left bundle-branch block.
I440	I44.0 — Atrioventricular block, first degree.
I441	I44.1 — Atrioventricular block, second degree.
I442	I44.2 — Atrioventricular block, complete.
I447	I44.7 — Left bundle-branch block, unspecified.
I45	Other conduction disorders.
I46	Cardiac arrest.
I47	Paroxysmal tachycardia.
I48	Atrial fibrillation and flutter.
I480	I48.0 — Paroxysmal atrial fibrillation.
I481	I48.1 — Persistent atrial fibrillation.
I482	I48.2 — Chronic atrial fibrillation.
I50	Heart failure.
IX.I60–I69	Cerebrovascular diseases (I60–I69).
IX.I70–I79	Diseases of arteries, arterioles and capillaries (I70–I79).
IX.I80–I89	Diseases of veins, lymphatic vessels and lymph nodes, not elsewhere classified (I80–I89).
IX.I95–I99	Other and unspecified disorders of the circulatory system (I95–I99).

Table 3: Extended ICD-10 code prediction performance by hierarchical group in the models studied in table 1. AUROC is reported for linear probing on each corresponding backbone.

	Ours		Baselines			
ICD hierarchy	**LAMAE**	**LAMAE$_E$**	**Scratch**	**MVMAE**	**Ind$_P$**	**Ind$_S$**
IX	*0.8345*	0.8340	0.7715	0.6771	**0.8380**	0.7776
IX.I05–I09	**0.8317**	*0.8278*	0.7408	0.5754	0.8259	0.7564
I07	*0.8772*	**0.8802**	0.8091	0.6804	0.8669	0.8310
I071	**0.8830**	*0.8740*	0.8236	0.6450	0.8609	0.8585
I078	*0.8818*	**0.8977**	0.8110	0.5145	0.8896	0.8345
I08	**0.8272**	0.8235	0.7523	0.6755	*0.8263*	0.7676
I080	*0.8345*	0.8318	0.7418	0.6619	**0.8390**	0.7513
I081	**0.8704**	*0.8695*	0.7719	0.7272	0.8556	0.7992
I083	**0.8852**	0.8573	0.8421	0.7311	*0.8847*	0.8742
IX.I10–I1A	*0.7549*	**0.7570**	0.7043	0.5861	0.7506	0.7092
I11	0.8103	*0.8124*	0.7491	0.6283	**0.8163**	0.7602
I13	*0.8651*	**0.8704**	0.8106	0.6826	0.8655	0.8194
I130	*0.8629*	**0.8687**	0.8183	0.7566	0.8668	0.8254
I132	*0.9009*	0.9096	0.7878	0.6384	**0.9171**	0.8089
IX.I20–I25	*0.7995*	**0.8046**	0.7425	0.6182	0.7939	0.7508
I20	0.7880	**0.7963**	0.7147	0.6574	*0.7934*	0.7324
I200	0.8236	**0.8269**	0.7366	0.6716	*0.8267*	0.7522
I209	*0.7925*	**0.8075**	0.7224	0.6796	0.7870	0.7414
I21	0.8229	**0.8402**	0.7465	0.5585	*0.8265*	0.7542
I210	*0.9330*	**0.9632**	0.9197	0.6276	0.9343	0.9143
I211	*0.9370*	**0.9588**	0.8049	0.6604	0.9269	0.8433
I213	0.8649	**0.8996**	0.8097	0.6387	*0.8814*	0.8010
I214	0.8043	**0.8117**	0.7350	0.6018	*0.8063*	0.7397
IX.I26–I28	0.7399	*0.7474*	0.6948	0.5785	**0.7499**	0.6977
IX.I30–I5A	0.8624	0.8624	0.7955	0.6321	**0.8665**	0.8010
I35	0.7981	**0.8050**	0.7365	0.6246	*0.7983*	0.7423
I350	0.8266	**0.8346**	0.7672	0.6112	*0.8268*	0.7784
I359	0.8444	*0.8525*	0.7397	0.6020	**0.8585**	0.7490
I42	*0.8772*	**0.8838**	0.8396	0.7193	0.8731	0.8458
I420	0.8914	*0.8986*	0.8463	0.7816	**0.9198**	0.8590
I428	*0.8851*	**0.8921**	0.8311	0.7144	0.8807	0.8392
I429	0.8586	*0.8611*	0.8020	0.6408	**0.8791**	0.8116
I44	0.9019	*0.9050*	0.8439	0.7591	**0.9091**	0.8467
I440	0.8984	*0.9102*	0.7545	0.6638	**0.9156**	0.7610
I441	0.8860	*0.9021*	0.8229	0.6309	**0.9147**	0.8338
I442	0.9113	*0.9151*	0.8498	0.7564	**0.9194**	0.8551
I447	0.9389	**0.9417**	0.9275	0.8633	*0.9397*	0.9305
I45	*0.8407*	**0.8493**	0.7766	0.6646	0.8392	0.7828
I46	0.8336	*0.8481*	0.7697	0.6562	**0.8523**	0.7809
I47	0.8051	*0.8023*	0.7409	0.6480	**0.8140**	0.7461
I48	0.8837	*0.8861*	0.7852	0.6952	**0.8927**	0.7933
I480	0.8059	*0.8135*	0.7301	0.6735	**0.8196**	0.7290
I481	0.8809	*0.8872*	0.8091	0.7141	**0.8875**	0.8152
I482	0.9228	*0.9206*	0.8040	0.7169	**0.9345**	0.8216
I50	*0.8720*	**0.8747**	0.8166	0.6169	*0.8720*	0.8235
IX.I60–I69	0.6694	*0.6723*	0.6290	0.5473	**0.6823**	0.6348
IX.I70–I79	0.7416	**0.7441**	0.6942	0.5956	*0.7440*	0.6974
IX.I80–I89	0.6890	*0.6949*	0.6349	0.5731	**0.6985**	0.6324
IX.I95–I99	0.6772	*0.6782*	0.6224	0.5519	**0.6943**	0.6275

Table 4: Extended ICD-10 code prediction performance by hierarchical group. Comparison of proposed LAMAE and LAMAE$_E$ under linear probing and fine-tuning of the corresponding pretrained backbone.

	Linear Probing		Fine-Tuning	
ICD hierarchy	**LAMAE**	**LAMAE$_E$**	**LAMAE**	**LAMAE$_E$**
IX	0.8345	0.8340	**0.8495**	*0.8486*
IX.I05–I09	0.8317	0.8278	**0.8509**	*0.8452*
I07	0.8772	0.8802	*0.8904*	**0.9039**
I071	0.8830	0.8740	**0.9044**	*0.8763*
I078	0.8818	0.8977	**0.9119**	*0.9099*
I08	0.8272	0.8235	**0.8490**	*0.8420*
I080	0.8345	0.8318	**0.8539**	*0.8425*
I081	0.8704	0.8695	**0.8936**	*0.8730*
I083	*0.8852*	0.8573	0.8794	**0.9163**
IX.I10–I1A	0.7549	0.7570	**0.7690**	*0.7678*
I11	0.8103	0.8124	**0.8343**	*0.8272*
I13	0.8651	0.8704	**0.8830**	*0.8798*
I130	0.8629	0.8687	**0.8817**	*0.8812*
I132	0.9009	*0.9096*	**0.9119**	0.9022
IX.I20–I25	0.7995	0.8046	**0.8282**	*0.8250*
I20	0.7880	0.7963	*0.8040*	**0.8183**
I200	0.8236	0.8269	**0.8445**	*0.8440*
I209	0.7925	0.8075	*0.8197*	**0.8217**
I21	0.8229	0.8402	**0.8773**	*0.8600*
I210	0.9330	**0.9632**	0.9615	*0.9631*
I211	0.9370	0.9588	**0.9749**	*0.9681*
I213	0.8649	0.8996	**0.9248**	*0.9043*
I214	0.8043	0.8117	**0.8584**	*0.8429*
IX.I26–I28	0.7399	0.7474	*0.7617*	**0.7682**
IX.I30–I5A	0.8624	0.8624	**0.8771**	*0.8759*
I35	0.7981	0.8050	**0.8244**	*0.8180*
I350	0.8266	0.8346	*0.8528*	**0.8644**
I359	0.8444	0.8525	**0.8681**	*0.8657*
I42	0.8772	*0.8838*	**0.8880**	0.8805
I420	0.8914	0.8986	**0.9170**	*0.8935*
I428	0.8851	0.8921	**0.8958**	*0.8932*
I429	0.8586	0.8611	**0.8809**	*0.8752*
I44	0.9019	*0.9050*	**0.9097**	*0.9053*
I440	0.8984	**0.9102**	0.8922	*0.9044*
I441	0.8860	*0.9021*	**0.9052**	0.8800
I442	0.9113	*0.9151*	**0.9184**	0.9095
I447	0.9389	*0.9417*	**0.9452**	0.9410
I45	0.8407	*0.8493*	**0.8519**	0.8442
I46	0.8336	0.8481	*0.8613*	**0.8634**
I47	0.8051	0.8023	*0.8106*	**0.8123**
I48	0.8837	0.8861	**0.9016**	*0.8993*
I480	0.8059	0.8135	*0.8201*	**0.8254**
I481	0.8809	*0.8872*	**0.8902**	0.8828
I482	*0.9228*	0.9206	**0.9312**	0.9285
I50	0.8720	0.8747	**0.8892**	*0.8857*
IX.I60–I69	0.6694	0.6723	*0.6836*	**0.6841**
IX.I70–I79	0.7416	0.7441	**0.7545**	*0.7456*
IX.I80–I89	0.6890	0.6949	*0.7121*	**0.7156**
IX.I95–I99	0.6772	0.6782	**0.6963**	*0.6939*